
Uncovering the topology of the medial temporal lobe in Alzheimer's disease.

Philip Hartout*

Department of Biosystems Science and Engineering
ETH Zürich
Zürich, Switzerland
phartout@ethz.ch

Abstract

Topological data analysis on medical imaging data is an emerging field leveraging the shape of data for various application domains, including machine learning tasks. Here, we apply a topological data analysis pipeline to uncover novel insights in the Alzheimer's disease neuroimaging initiative dataset by applying persistent homology on a patch of the medial temporal lobe to extract persistence images and persistence landscapes. We use these representations to (i) learn to classify patients suffering from Alzheimer's disease from cognitively normal patients thereby assessing the saliency of persistence images extracted from the most affected brain regions in Alzheimer's disease, (ii) analyze the topological heterogeneity of each of the diagnostic categories, as well as (iii) across various time points available for each patient. Finally, we use these representations to (iv) cluster the patients according to their diagnosis and disease subtypes, when applicable.

A graphical abstract of the analyses discussed in this report is shown in Figure 1

1 Introduction

1.1 Alzheimer's disease

Alzheimer's disease (AD) is the most prevalent form of dementia in the world, with a forecasted 75 million cases in 2030 and 132 million by 2050 [WHO, 2017]. In EU member states and Switzerland, AD is already among the leading causes of death and is projected to further accelerate in the future [Sleeman et al., 2019]. The associated costs are immense—in the United States alone, the cost of care of AD patients is expected to be \$2 trillion by 2030—, and are poised to substantially burden the economic prosperity of developed countries in the future [WHO, 2017]. Although the definite diagnosis of a patient with AD can only be done post-mortem, clinicians use a plethora of standardized tools to find indications of the developing pathology as early as possible, ranging from neuropsychological tests, blood and cerebrospinal fluid biomarkers, to MRI images [McKhann et al., 2011, Smits et al., 2012, Lehmann and Teunissen, 2016].

Although there are disputes on the root cause of the disease in the late-onset form of AD [Tharp and Sarkar, 2013, Fulop et al., 2018, Hur et al., 2020], there is a wide consensus that the presence of Amyloid β ($A\beta$), originating from cleavage of the amyloid precursor protein (APP), together with the aggregation of neurofibrillary tangles, stemming from hyperphosphorylated tau proteins, accumulate in the brain of patients with AD and leads to neural cell death [Dá Mesquita et al., 2016]. This cellular destruction leads to a cumulative effect: brain atrophy, which refers to the shrinkage of brain volume. This damage particularly affects brain regions involved in memory formation such as

*With thanks to Bastian Rieck for the supervision and Sarah Brueningk, Felix Hensel, Catherine Jutzeler, Merel Kuijs, and Louis Lukas for insightful discussions, code, and data. Last compiled: January 7, 2021

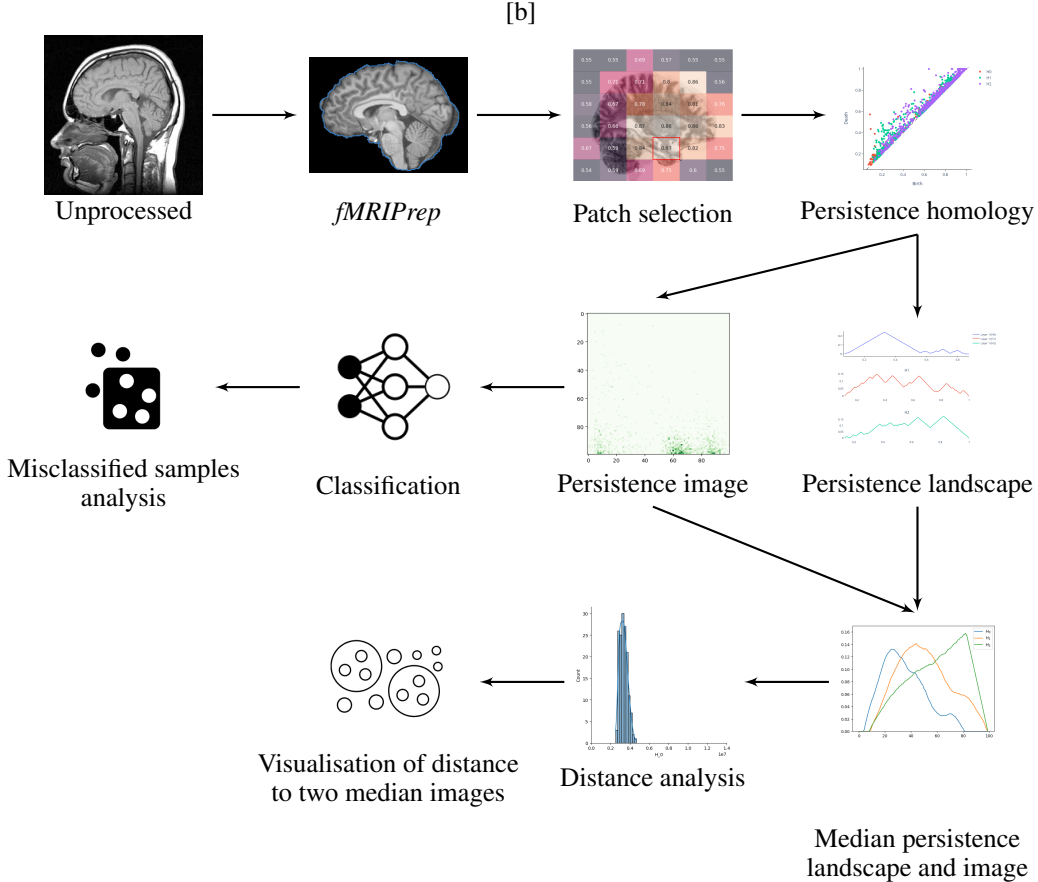


Figure 1: Flow chart of the analyses conducted in this report. Images adapted from [Wikimedia](#), [slicer.org](#), [Xela Ub](#) and [Sachin Modgekar](#)

the medial temporal lobe (MTL), which contains the entorhinal cortex, the hippocampus, and the amygdala [Goedert and Spillantini, 2006] is visible using structural Magnetic Resonance Imaging (sMRI) [Frisoni et al., 2010], and has been heralded as one of the most reliable biomarkers for Alzheimer’s disease [Pini et al., 2016].

Such images provide a rich source of data, which can then be used for various purposes. One of them is classification, which consists of categorizing cognitively intact subjects (CN) and AD patients using deep learning techniques such as convolutional neural networks [Wen et al., 2020]. Additionally, sMRI data can be used to identify multiple regions affected by the disease, and patterns have emerged as to which groups of regions are affected, leading to the definition of various subtypes of AD [Poulakis et al., 2018, Tijms et al., 2020]. To gain even finer insights from the observable alterations of brain shape in the context of AD with minimal computation, ideas stemming from the mathematical field of topology can be applied. Topology concerns itself with properties of geometric objects under continuous deformations, such as stretching, twisting, crumpling, and bending. Such deformations aptly summarize the type of deformation occurring to the brain due to AD and therefore makes an ideal context in which we can apply computational topology to uncover and quantify anatomical changes resulting from the disease.

1.2 Topology

Topology has witnessed relentless theoretical progress since Henri Poincaré first addressed topological ideas as a distinct branch of mathematics in his 1895 publication of *Analysis Situs* [Poincaré, 1895, James, 1999]. Only recently, – with the advent of modern computing – has the field of computational topology and topological data analysis (TDA) gained momentum to investigate (high-dimensional)

data in physics, biology, and beyond [Dey et al., 1999, Ghrist, 2008, Amézquita et al., 2020]. While surveying the various applications of computational topology are beyond the scope of this report, we still want to define several procedures that are paramount to the workflow described in this report: cubical persistence, various vectorized representations of the persistence diagrams obtained from filtered cubical complexes, and the notion of pairwise distance between such representations. For material providing an extensive and formal introduction to topology and persistent homology, please refer to Freedman and Chen [2009], Edelsbrunner and Harer [2010], Ghrist [2008].

1.2.1 Cubical complexes and persistent homology

Before defining the notion of cubical persistence, *cubical complexes* need to be defined. For that, let us first assign to each elementary non-degenerate interval for some $[a, a + 1] \forall a \in \mathbb{R}$, two degenerate intervals $[a, a]$ and $[a + 1, a + 1]$. For a d -dimensional space, a cube is then defined as a product of d elementary intervals $\prod_{i=1}^d I_i$. The dimension of the cube is then equal to the number of non-degenerate interval in the aforementioned product, such that 0-cubes, 1-cubes, 2-cubes, and 3-cubes correspond to vertices, edges, squares, and 3D cubes, respectively. In this report, the 3D cube corresponds to a given voxel of our sMRI.

A cubical subcomplex X of dimension d is then defined as a finite set of elementary cubes of at most dimension d , where X must be closed undertaking faces and intersections, i.e. for any cube in X , all of its faces must belong to X , and for any two cubes in X , their intersection is either empty, or there is a common face between them.

To obtain the entire cubical complex \mathbb{X} contained in an sMRI image of a particular patient taken at a particular timepoint, we use a filtering function $f : \mathbb{X} \rightarrow \mathbb{R}$ (such as an activation function), which corresponds to the pixel density of each voxel, to study the topology of the sublevel sets $\mathbb{X}_t = f^{-1}(-\infty, t]$ of cubical subcomplexes that arise. This is a method to study topological spaces referred to as *persistent homology*. A common representation of the evolution of topological complexes as a function of the value of the filtration function is the *persistence diagram* (PD), which is a multiset of points. For each homological dimension (here, 0, 1, 2), we obtain a collection of points, with an associated x and y coordinate which corresponds to the birth and death of a topological feature in the homology dimension $n = 0, 1, 2, \dots$, respectively. The homological dimensions 0, 1, 2 can be interpreted as connected components, tunnels and cubes, respectively. We refer to a homological feature as *persistent* if the difference between its birth and death value is particularly high.

1.2.2 Persistence images and persistence landscapes

PDs are endowed with a metric (further discussed in Section 1.2.3), so it is possible to perform a variety of machine learning (ML) techniques using representations of PDs as input data. However, multiple ML algorithms require more than a metric –fixed-size vectors are often required–. It is therefore desirable to have a fixed-length, stable, efficient-to-compute, interpretable (with respect to the PD) and tunable mapping from the PD to a vector space in \mathbb{R}^n to fit various machine learning algorithms to them.

One such representation is the *persistence image* (PI) of a PD, which has also been proven to be stable upon small perturbations of data while still retaining the underlying features in the data useful for classification. Computing the PI from a PD D consists of a two-step process. First, the PD is mapped to an integrable function $\rho_D : \mathbb{R}^2 \rightarrow \mathbb{R}$ called a persistent surface. This surface is a weighted sum of Gaussian distributions, each centered around a point of the PD. The matrix of pixel values can be obtained from the computation of the integration of ρ_D on a grid overlaid on the surface Adams et al. [2017]. An overview of the pipeline to obtain persistence images is shown in Figure 2.

Another representation associated to the PD is the persistence landscape (PL). Similarly to PIs, PLs maps the PD into a Hilbert space as well, which is useful for ML applications, but additionally extracts the most persistent features of the data. In order to define a persistence landscape, let us take a pair (b, d) , which refer to the birth and death of a topological feature. We now define the piecewise linear function $f_{(b,d)} : \mathbb{R} \rightarrow [0, \infty]$ as

$$f_{(b,d)}(x) = \begin{cases} 0 & \text{if } x \notin (b, d) \\ x - b & \text{if } x \in (b, \frac{b+d}{2}] \\ -x + b & \text{if } x \in (\frac{b+d}{2}, d] \end{cases} \quad (1)$$

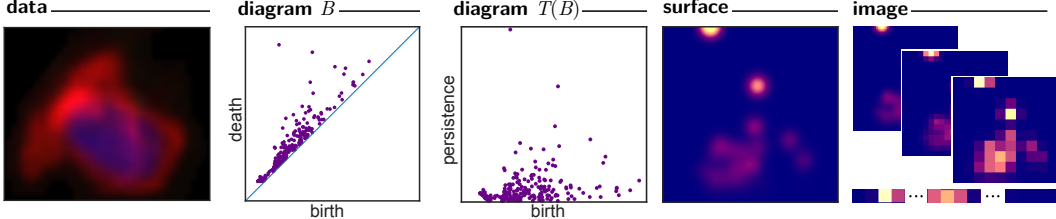


Figure 2: Pipeline to obtain the persistence image, as presented by Adams et al. [2017].

The PL of the birth-death pairs $\{b_i, d_i\}_{i=1}^n$ is the sequence of functions $\lambda_k : \mathbb{R} \rightarrow [0, \infty]$, $k = 1, 2, 3, \dots$ where $\lambda_k(x)$ is the k^{th} largest value of $\{f_{b_i, d_i}(x)\}_{i=1}^n$. We set $\lambda_k(x) = 0$ if the k^{th} largest value does not exist, which results in $\lambda_k = 0$ for $k > n$ [Bubenik, 2015, 2020].

1.2.3 Pairwise distances and medians

A crucial element in our investigations consists of examining distances between vectorized topological representations. Intuitively, and as noted by [Berwald et al., 2018], it is important to take the meaning of the points of the PD into account; namely that a point close to the diagonal ($c, c + \epsilon$) represents a feature that lived for a short time ϵ . A diagram with this small lifetime point should therefore be close to the same diagram without that point, where the feature would not appear at all. Hence, it makes sense to introduce the notion of minimal cost required to match up points of the two diagrams, either off-diagonal to off-diagonal, or off-diagonal to the nearest point on the diagonal (for small values of ϵ). In this context, distance functions usually applied to evaluate the distance between two probability density distributions are relevant: the bottleneck distance and the p -Wasserstein distance, where $p \geq 1$. The p -Wasserstein distance between two diagrams D_1 and D_2 is the infimum over all bijections $\gamma : D_1 \cup \Delta \rightarrow D_2 \cup \Delta$, where Δ is the multiset $\{(s, s) \mid s \in \mathbb{R}\}$ with multiplicity $(s, s) \mapsto +\infty$, of

$$\left(\sum_{x \in D_1 \cup \Delta} \|x - \gamma(x)\|_q^p \right)^{1/p} \quad (2)$$

where we usually have $q = \infty$. When we let $p \rightarrow \infty$, we recover the bottleneck distance.

We also use the notion of a median persistence landscape, where, given a collection of PDs, we compute their associated binned PL, which is a matrix of fixed dimension $m \times h$ where m is the length of the binned λ_1 persistence landscape, and h is the homology dimension. We compute the median PL by taking the median over all samples for each cell in m for each homology dimension h , so we end up with a PL representative of the collection of the samples in the collection. A similar approach can be adopted for PIs. The median PL and PI were chosen over the average PL or PI due to the skewed distribution of the data observed in some cases, as will be highlighted in section 4.2.

Taking the distance between any two persistence landscapes or images can be achieved using the Minkowski distance—essentially a proxy for the p -Wasserstein distance for fixed-length vectors. We define the Minkowski distance given two vectors $\mathbf{x}, \mathbf{y} \in \mathbb{R}^n$, as:

$$D(\mathbf{x}, \mathbf{y}) = \left(\sum_{i=1}^n |x_i - y_i|^p \right)^{\frac{1}{p}}. \quad (3)$$

In this report, we set $p = 1$ and henceforth refer to the distance function as the L^1 norm.

1.3 Research questions and outline

In this report, we address the following research questions:

1. How salient are the topological features extracted from the patch for the characterization of the atrophy observed in Alzheimer's disease as measured through the classification performance of AD versus CN subjects using persistence images?

2. What does the distance between the persistence image and persistence landscape of a patient and the median persistence image or landscape of a diagnostic category reveal about the topological heterogeneity within a given diagnostic category?
3. How can the distance among persistent images taken for each patient over the course of the disease inform us with regard to the progression of the patient during the monitoring period?
4. Does taking the distance between each image and two median persistence images (from AD patients and CN subjects) allow adequate clustering of patients in diagnostic categories or disease subtypes?

This report is structured as follows: after having introduced AD and fundamental concepts related to TDA in this introduction, we go on to present and justify methodological choices we have made regarding the topological data analysis conducted on sMRI data in section 2; in section 3, we report the findings extracted from the data, which we discuss in section 4.

2 Methods

Here, we present the methodological choices made for this pipeline. All of the code used to compute the findings presented in this paper is currently available upon request on [GitHub](#).

2.1 Data

T1-weighted, 1.5 Tesla sMRIs were obtained from the [Alzheimer’s Disease Neuroimaging Initiative](#) (ADNI) database which contains images from AD patients, patients diagnosed with mild cognitive impairment (MCI) [Gauthier et al., 2006], and healthy controls (cognitively normal, CN) of matched age groups [Jack Jr et al., 2008]. Further preprocessing steps to reduce noise and extract brains structures is highlighted in appendix A.1. Then, scans were divided into 216 patches, each of dimension $30 \times 36 \times 30$, providing a possibility for a more focused and computationally efficient investigation while preserving high resolution. Working with a patch is also supported by the fact that an investigation of *local* changes in brain architecture may filter out topological features that are less relevant in the context of Alzheimer’s disease.

From earlier work attempting to classify CN subjects from AD patients using a convolutional neural network (CNN) [Brüningk et al., 2020], we know that a given patch, shown in grey in figure 3, has a particularly high discriminatory potential, so we selected this patch for all our further analyses. Support for the use of this patch also comes from its anatomical relevance, since it contains regions that are most affected in Alzheimer’s disease such as the hippocampus, the entorhinal cortex, and the amygdala [Goedert and Spillantini, 2006].

2.2 Topological Data Analysis

To perform the topological analysis on the patch, we used `giotto-tda`, a library specifically made for the integration of TDA pipelines in ML applications [Tauzin et al., 2020]. Each filtration on the cubical complexes has been done in three homological dimensions 0, 1, 2, representing features in each of the dimensions of the three-dimensional image. We otherwise used the default parameters provided by the [giotto-tda documentation](#). An example persistence diagram for a cognitively intact subject, a patient with MCI, and a patient with AD are depicted in Figure 4. To obtain persistence images for each 3D volume, we used 0.001 as a standard deviation for the Gaussian kernel, no weight function, and a default dimension of 100×100 for each image. The stability of the performance of the classifier shown below was the highest at these particular values, although image dimensions did not really influence the performance of local patches, however higher values for the standard deviation of the Gaussian kernel seemed to affect performance beyond 0.1. Representative samples of these images are shown in Figure 6.

2.3 Model architecture

For the classification task of classifying AD vs CN patients, we used a parallel CNN network with one convolutional layer, followed by one dense layer containing 500 neurons and with dropout rates of 50% at training time. The output of the last dense layer is redirected to a single sigmoid neuron

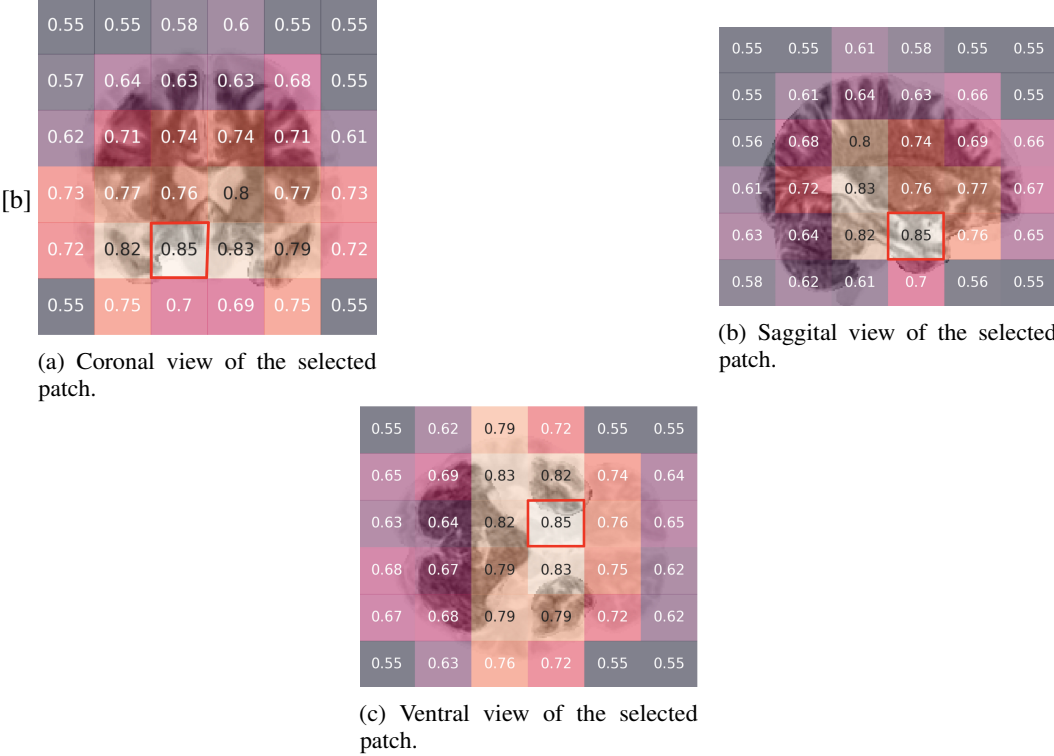


Figure 3: Accuracy values on each patch. The selected patch is boxed in red.

for prediction. The model was trained using an exponential decay learning rate scheduler and early stopping, which monitored the validation loss. All of the layers and utilities to train the neural network were provided by the Keras library [Chollet et al., 2015] and are available on the [repository](#), and a depiction of the computation graph is shown in Figure 5. We also note that the model was trained on a laptop CPU (Intel(R) Core(TM) i7-9750H CPU @ 2.60GHz). For consistency and to enable a direct comparison with results shown in [Brüningk et al., 2020], we used the same data partitioning to present any kind of data leakage that would artificially increase our score, as discussed in Wen et al. [2020]. We also computed persistence images with the same parameters from the entire brain in scan projected in MNI space and trained a separate network with the same parameters. Each model was trained three times to mitigate any performance fluctuations due to different layer initializations.

2.4 Distance between median topological representations

We also used `giotto-tda` to compute persistence landscapes. We wanted to keep only the most prominent features, so we kept only λ_1 , and set the PL vector lengths of 100. The median PL for each homological dimension is shown in Figure 7.

Computing the median persistence landscape for each diagnostic category was done using the median value of each subject for each of the vector coordinate. The pairwise distance between two PLs was taken using the L^1 norm.

We compute the distances in two settings:

Intra-diagnostic category setting : here, we compute the distance of each PL available for all available sMRIs belonging to a diagnostic category with respect to the median PL of that category. For this particular analysis, we extracted the earliest available image for that patient. Additionally, we check whether or not the distribution of the distances is skewed by performing a Shapiro-Wilk test of normality. A significant p -value—defined at $\alpha < 0.05$ —for this test indicates evidence that the distribution is not normal, and that it is skewed.

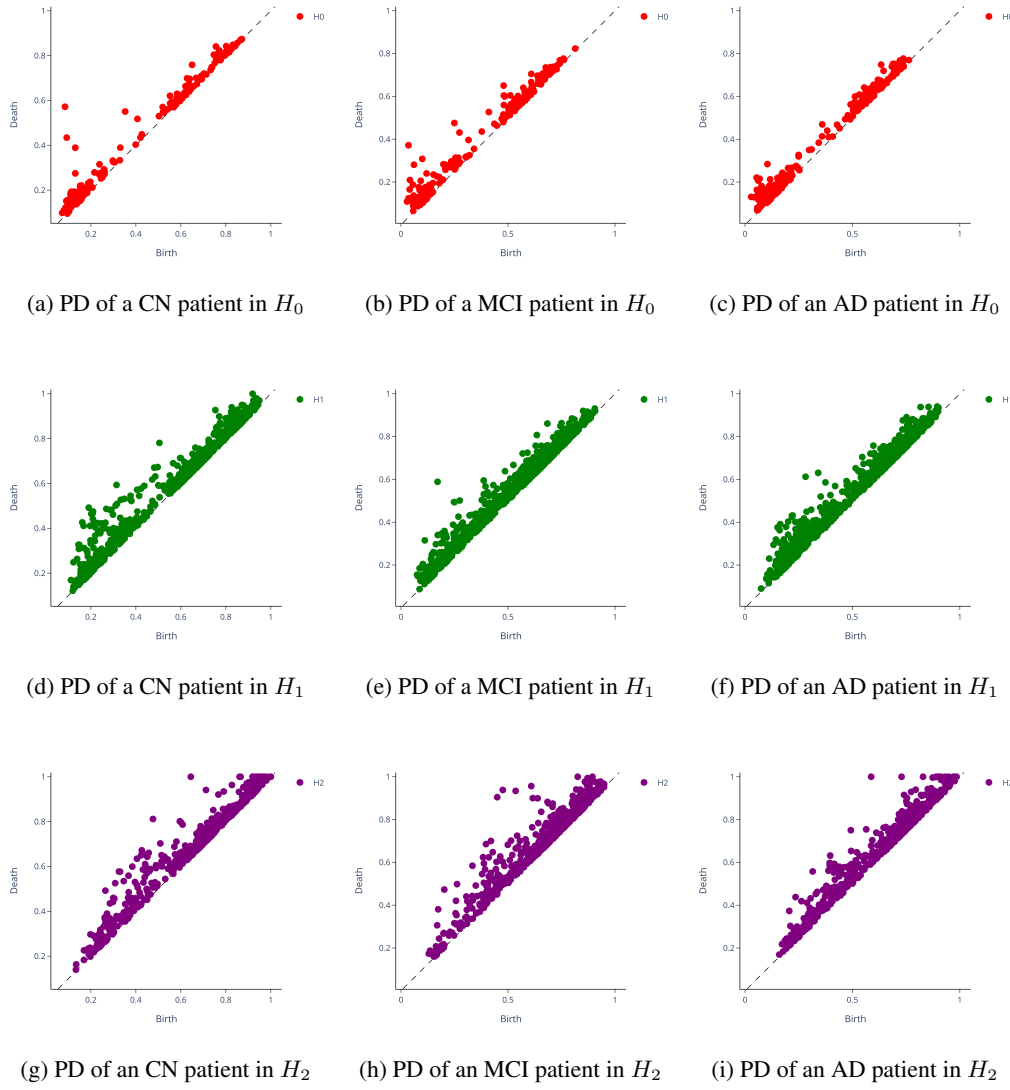


Figure 4: Representative PD for each of the diagnostic categories.

Intra-patient distance : this allows us to assess the distance of the different PDs of the same patient, to see if there is any distinctive evolution of the topological features over time. In this context, we compute the pairwise distances for all sMRIs from a patient. For some analyses, we averaged the pairwise distance for each patient, and grouped patients that changed diagnosis over time in one category, and those that did not in another. Additionally, the unpaired Mann-Whitney \mathcal{U} test was used to test whether the distributions of distance values depending on whether or not the patient changed diagnosis over the course of the time images were taken stem from the same latent distribution [Mann and Whitney, 1947].

We performed each of the analyses on both persistence landscapes and images to highlight differences among persistent features in the case of the persistence landscapes and all of the topological features in the case of the persistence image.

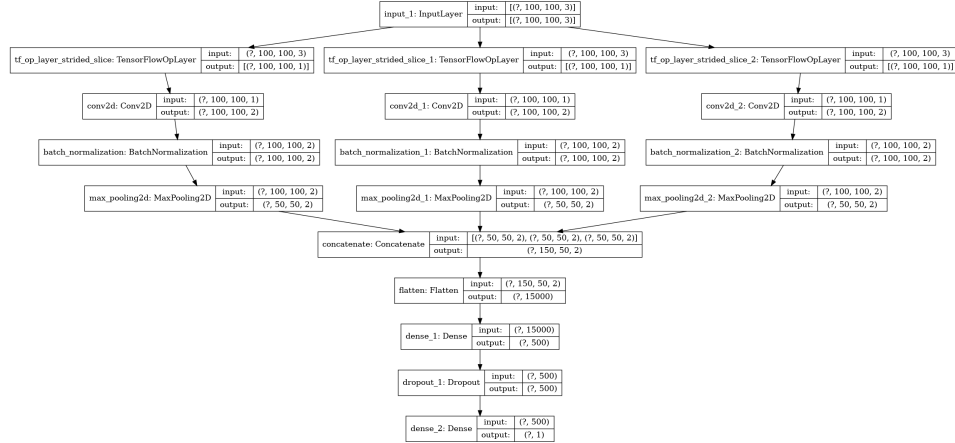
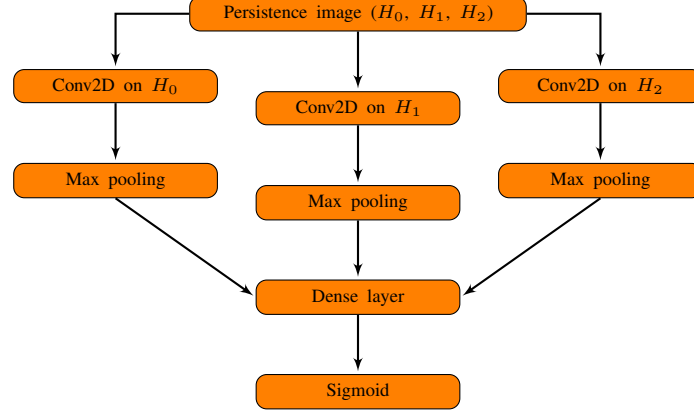


Figure 5: Computation graph to predict the phenotype of a given set of persistent images derived from applying persistent homology to an sMRI image. The top diagram is a simplified representation of the output of the Keras `plot_model()` function, shown below.

2.5 Relationship between distances and misclassification

To investigate the relationship between patients departing significantly from the median representation of the diagnostic category to which they belong and misclassified patients, we chose to take the n subjects – hereafter referred to as *topological outliers* – with the highest L_1 norm from their median representation, and set n to the number of misclassified patients from one trained network defined in section 2.3 – here, 145 images were misclassified. We then looked at the overlap between patients who were misclassified and the selected set of topological outliers, as well as the distribution of the distance of the misclassified samples compared to the median representation.

2.6 Clustering using multiple median topological representations

As the last step, we investigated whether the distance of a patient with respect to more than one median persistence image. We, therefore, evaluated the L^1 norm between each persistence image and both the median AD persistence image and median CN persistence image in H_2 (i.e. voids). We chose to take these two images because they showed high variability in other analyses (see Figure 10) and they represent the two most divergent diagnostic cases in our dataset, MCI being considered as a state where patients are neither cognitively normal nor formally diagnosed with AD. Given we

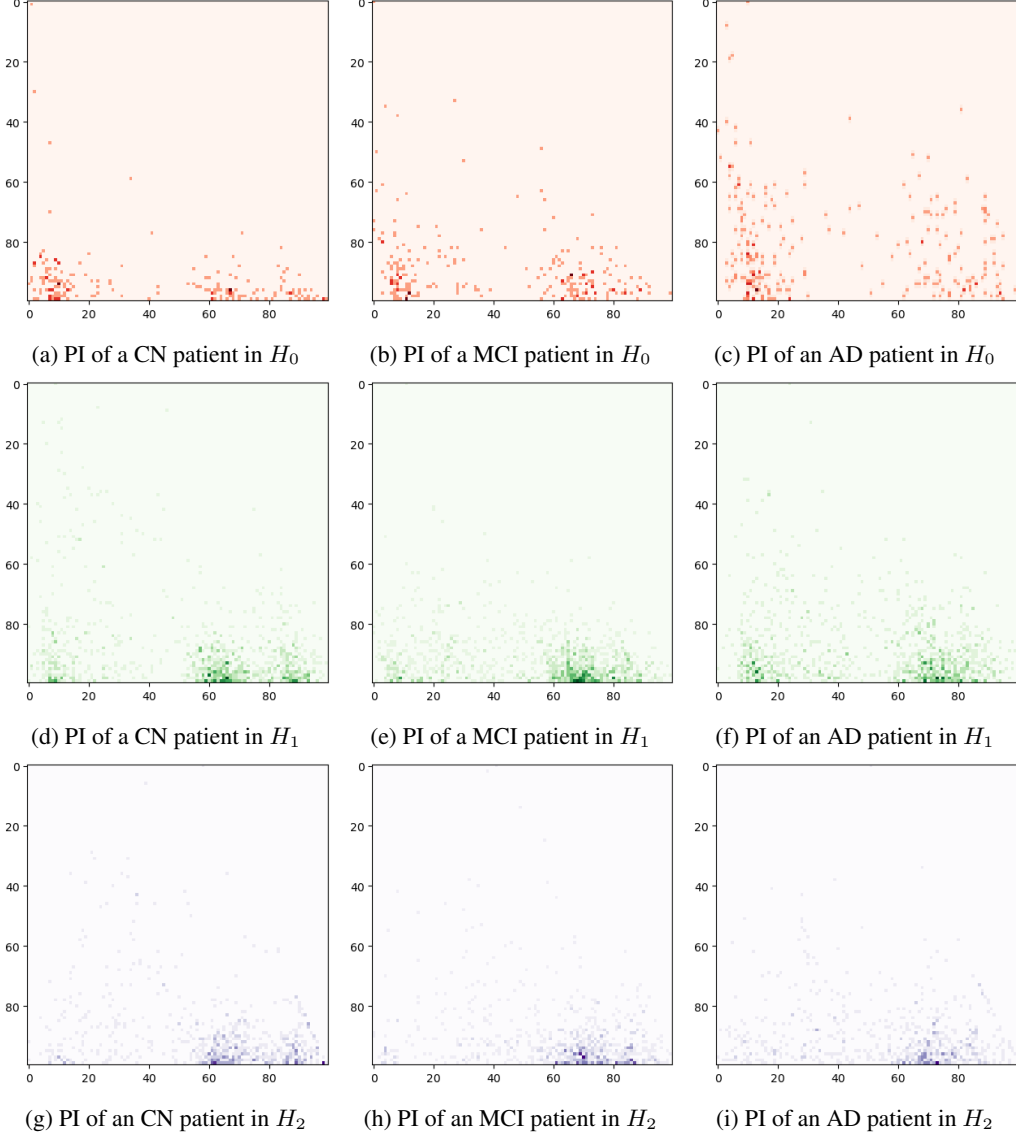


Figure 6: Representative PI for each of the diagnostic categories. Each column corresponds to a diagnostic category whereas each row corresponds to a homological dimension.

wanted to maximize variance across samples for visualization purposes, we first standardized the data and subsequently applied a principal component analysis to the resulting pairs of distances.

3 Results

Here we present the results obtained from the above-mentioned pipeline, starting with a performance assessment of the deep learning model. We then turn our attention to the topological heterogeneity observed both within each diagnostic category and within each patient. We then present our findings of the overlap between topological outliers and misclassified samples. Finally, we look at the distance of each image to the median image representation of AD and CN to see if clusters emerge.

3.1 Model Performance

The performance metrics of the deep learning model is shown in Table 1, and seems to be somewhat inferior to state-of-the-art models trained on similar data [Wen et al., 2020], but requires dramatically

less computing power – the relatively shallow multilayer CNN shown in Brüningk et al. [2020], for instance, requires 15 minutes of training time on a server GPU while our approach requires only 2 minutes on one laptop CPU, showing the high grade of compression of the approach presented here. Additionally, the model yields higher results compared to whole-brain persistence images reported in [Brüningk et al., 2020] as well as when training the network on whole-brain PIs obtained with the same parameters. Theoretically, the information contained in a patch PI should be contained in a whole-brain PI, so reducing the standard deviation of the Gaussian kernel as well as computing larger patches should be preferred. Remarkably, we observe that the performance of our network seems to be more stable than other approaches for which standard deviations of performance metrics are provided.

3.2 Distance analysis

3.2.1 L^1 norm among diagnostic categories – topological heterogeneity of each diagnostic category

We now present our findings regarding the distribution of the distances between the PL and PI of each image with respect to the median PL and PI for each diagnostic category. The representative PL and PI for each diagnostic category is shown in Figure 7 and 8, and the distribution of the L^1 norm between each patient and these median PLs and PIs is shown in Figure 9 and Figure 10, respectively. As we can see, while the median PLs do not differ too much from one another in each of the homological dimensions, we see that some persistence images seem to have a far greater distance to this median PL than the majority of PLs. This is also reflected by the skewness of the distributions observed in Figure 9 and confirmed in the skewness values shown in Table 2. Additionally, both the Shapiro-Wilk test and Kolmogorov-Smirnov tests for normality were significant, showing the data is not sampled from a normal distribution. However, the skewness of the distribution does not appear when looking at the distribution of distance values between PIs, except for AD patients, where skewness values remain high (Figure 10 and Table 3).

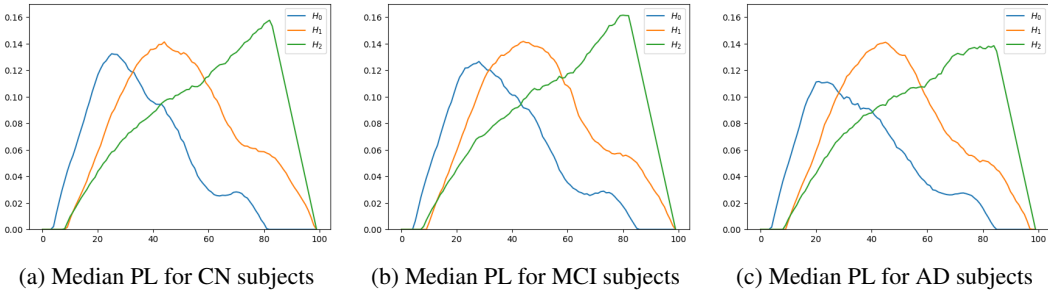


Figure 7: Median persistence landscapes for each of the diagnostic categories.

	Local (single patch)	PI	3D Conv	PI	SOTA
	Global (whole-brain)	PI	PI	PI	
Validation accuracy	0.79 ± 0.02	0.74 ± 0.03	0.85 ± 0.06	0.76 ± 0.02	0.91
Precision	0.81 ± 0.04	0.80 ± 0.05	0.78 ± 0.04	0.87 ± 0.04	-
Recall	0.81 ± 0.02	0.85 ± 0.08	0.87 ± 0.08	0.88 ± 0.08	0.84
AUC	0.85 ± 0.03	0.77 ± 0.03	0.89 ± 0.05	0.78 ± 0.02	0.96

Table 1: Performance metrics of the local PI approach. Bold column headers represent performance numbers obtained from the networks trained in this report. Global PI and local 3D Conv approach as reported from Brüningk et al. [2020]. SOTA results are obtained from Liu et al. [2018].

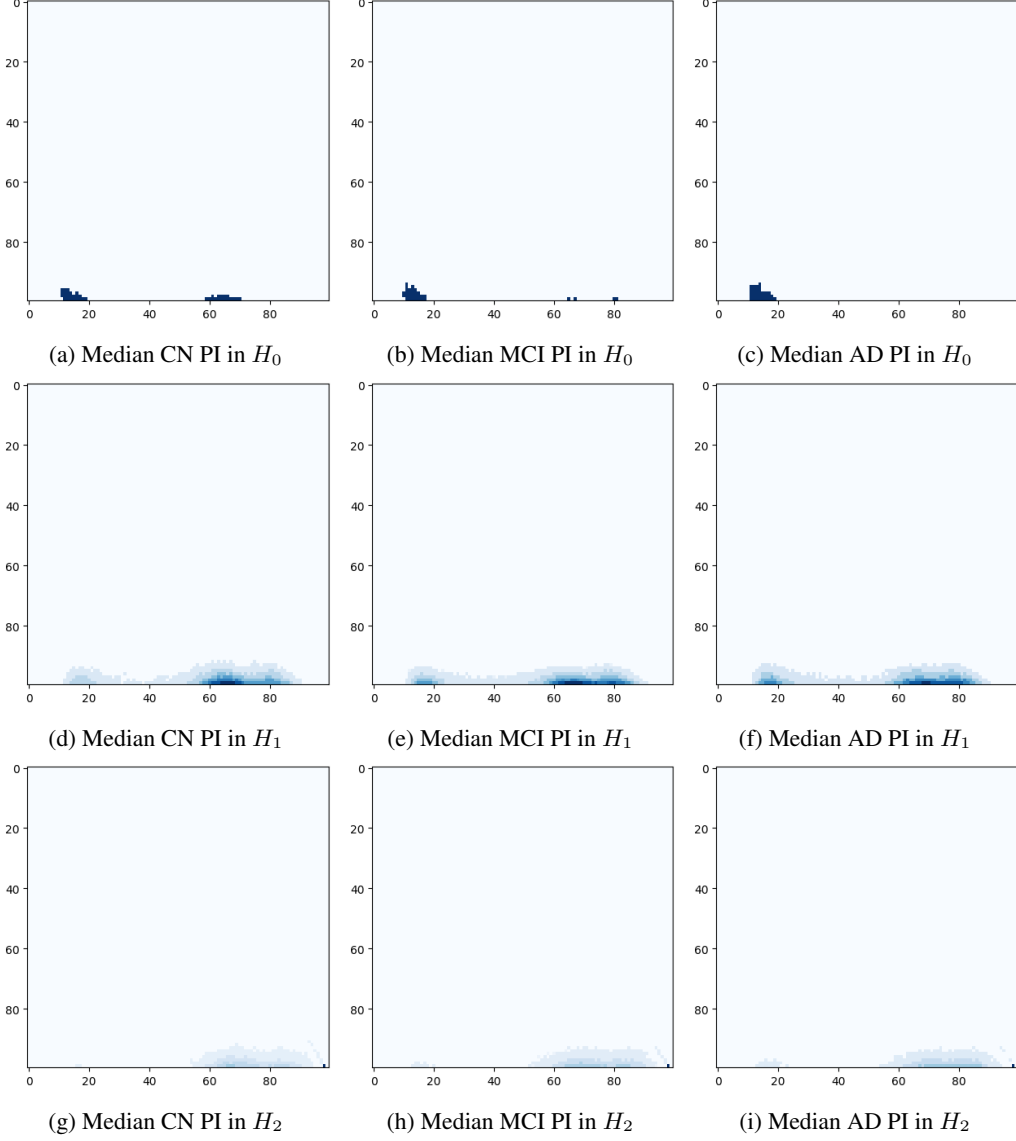


Figure 8: Median persistence images for each of the diagnostic categories and homological dimension.

3.2.2 Intra-patient pairwise distance and average L^1 norm distributions – topological evolution

As indicated in section 2.2, we can compute the distance between various PLs associated with the different timepoints available to a single patient to evaluate the distance between each of these topological representations at these timepoints, hence obtaining a representation of the topological evolution of that particular patient. When applying this approach to our data, we find interesting qualitative results: distances varying widely from one patient to the next. For instance, if we take a CN patient diagnosed as such throughout the time that patient has been monitored, we see relatively low distances between that patients and other timepoints – see Figure 11 for an example. However, distances seem higher when taking a patient who transitions from an MCI diagnosis to an AD diagnosis, as can be seen in Figure 12. Note that the color scale is the same for Figures 11 and 12. However, these effects do not generalize: if we take the average distance for each homological dimension for each patient and compare the distribution of these averages for patients who deteriorate (i.e. transition from CN to MCI or from MCI to AD) and those who do not, we do not see any quantitative difference, as can be seen in Figure 13. Surprisingly, we see that taking the average

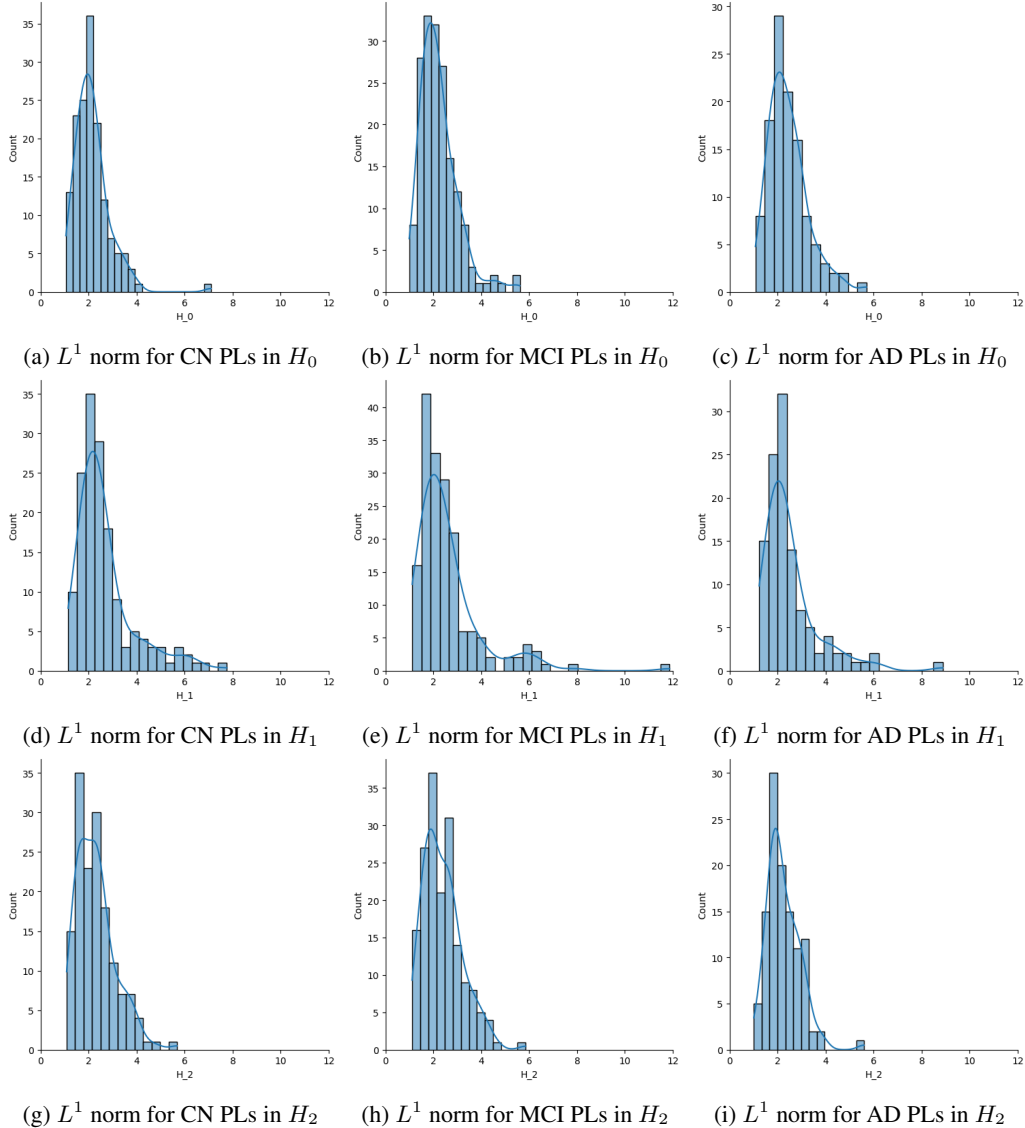


Figure 9: Histogram showing the distribution of the L^1 norm taken between the median PL for a diagnostic categories in all homological dimensions.

Wasserstein distance for each patient, a bimodal – similar for both deteriorating and stable patients – distribution arises, but mostly disappears as we let $p \rightarrow \infty$ and recover the bottleneck distance. The cause of the distance change is not known. Additionally, while no substantial differences are observed, we do see slight rightwards shifts in each mode for both Wasserstein and the L^1 norm of the persistent landscape, indicating a potentially increased distance distribution among some of the observed data points. Performing a Mann-Whitney \mathcal{U} test on the data confirms this qualitative finding, by showing that the two distributions shown in Figure 13 stem from two different latent distributions ($p < 0.01$ for all distributions).

3.3 Topological outliers and misclassified samples.

The distribution of distances with respect to the average persistent landscape was plotted for the patients who were correctly classified, and for those who were not correctly classified. The results are shown in Figure 14. We also examined the proportion of patients who switched diagnoses in the whole ADNI dataset. We found that 70% (64) of the misclassified patients had only one diagnosis

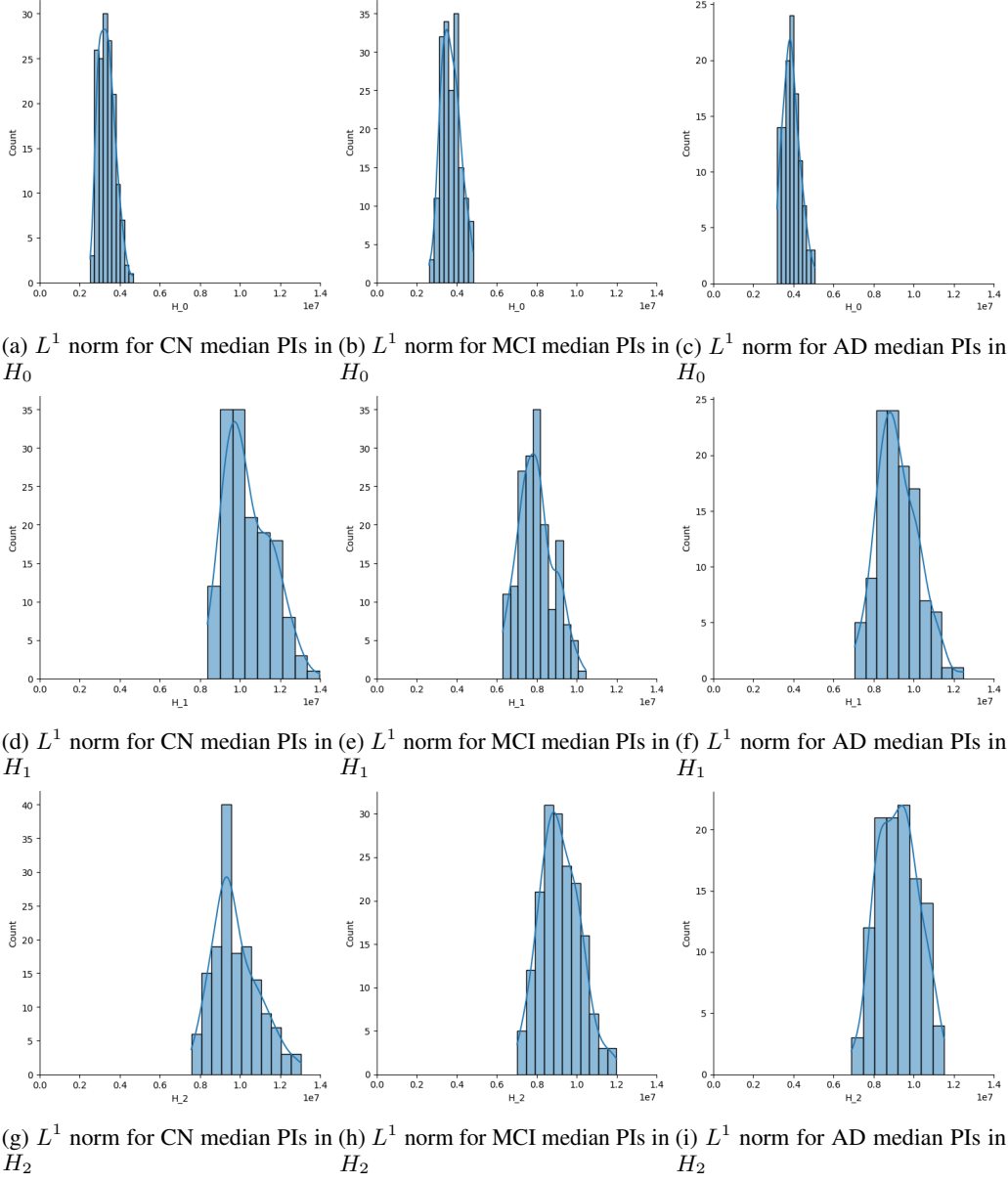


Figure 10: Histogram showing the distribution of the L^1 norm taken between the median PI and each image within a diagnostic category in all three homological dimensions.

versus 71% (323) in the whole dataset, hence indicating that misclassified patients did not contain persistent features that made them more likely to be misclassified.

3.4 Visualisation of the distance of each patient to the median PI of AD patients and CN patients

The results of the procedure highlighted in section 2.6 is shown in Figure 15. We see that on average AD patients tend to cluster higher up in the visualization compared to CN subjects. As expected, patients diagnosed with MCI tend to comingle among AD and CN patients. Clear clusters need yet to be defined more clearly using topological data analysis.

	Mean	Median	Std. dev.	Q3	Max	Skewness	SW
CN H_0	2.145	2.022	0.74	2.457	7.095	2.351	1.9×10^{-11}
CN H_1	2.669	2.35	1.202	2.9	7.757	1.823	7.2×10^{-13}
CN H_2	2.293	2.198	0.812	2.647	5.677	1.093	4.6×10^{-7}
MCI H_0	2.215	2.063	0.78	2.559	5.609	1.52	6.0×10^{-10}
MCI H_1	2.592	2.219	1.407	2.85	11.866	2.787	2.4×10^{-16}
MCI H_2	2.382	2.251	0.815	2.782	5.852	0.95	2.2×10^{-6}
AD H_0	2.422	2.261	0.813	2.832	5.701	1.189	1.1×10^{-5}
AD H_1	2.514	2.183	1.172	2.717	8.878	2.395	3.6×10^{-12}
AD H_2	2.237	2.073	0.686	2.637	5.594	1.305	6.1×10^{-6}

Table 2: Summary statistics of the distribution of distances from median persistence landscapes for each diagnostic category shown in Figure 9. Highlighted values represent relatively high values. SW: Shapiro-Wilk test p -value

	Mean	Median	Std. dev.	Q3	Max	Skewness	SW
CN H_0	3.3×10^6	3.3×10^6	4.0×10^5	3.6×10^6	4.6×10^6	5.2×10^{-1}	0.006
CN H_1	1.0×10^7	1.0×10^7	1.1×10^6	1.1×10^7	1.4×10^7	6.7×10^{-1}	0.0
CN H_2	9.7×10^6	9.4×10^6	1.1×10^6	1.0×10^7	1.3×10^7	6.4×10^{-1}	0.0
MCI H_0	3.6×10^6	3.6×10^6	4.6×10^5	4.0×10^6	4.8×10^6	2.5×10^{-1}	0.071
MCI H_1	7.9×10^6	7.8×10^6	8.7×10^5	8.4×10^6	1.0×10^7	3.5×10^{-1}	0.018
MCI H_2	9.1×10^6	9.0×10^6	9.9×10^5	9.8×10^6	1.1×10^7	3.4×10^{-1}	0.169
AD H_0	3.8×10^6	3.8×10^6	4.1×10^5	4.1×10^6	5.0×10^6	4.8×10^{-1}	0.034
AD H_1	9.1×10^6	9.0×10^6	1.0×10^6	9.9×10^6	1.2×10^7	4.4×10^{-1}	0.144
AD H_2	9.2×10^6	9.1×10^6	1.0×10^6	9.9×10^6	1.1×10^7	1.0×10^{-1}	0.387

Table 3: Summary statistics of the distribution of distances from median persistence image for each diagnostic category shown in Figure 10. Highlighted values represent relatively high values. SW: Shapiro-Wilk test p -value.

4 Discussion

In this section, we begin by discussing how persistence images provide salient features for the characterization of atrophy due to Alzheimer’s disease and result in competitive classification performance results; we then move on to discuss our findings regarding the distributions of distances among diagnostic categories and within patients, also touching upon how distances relate to misclassified samples. Then, we briefly discuss how taking the distance of each image with respect to two median persistence images yields trends of clusters of patients. Finally, we outline some limitations and further research avenues to be explored in the future.

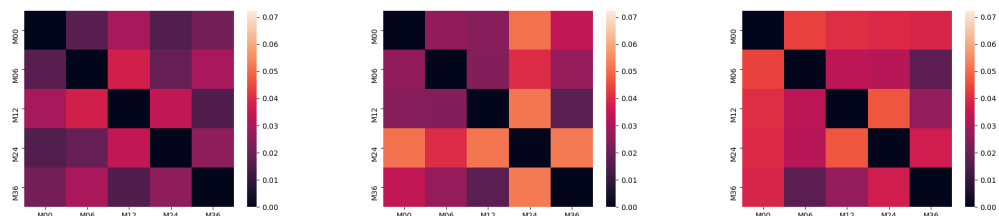


Figure 11: Topological evolution of a subject with an unchanging CN diagnosis.

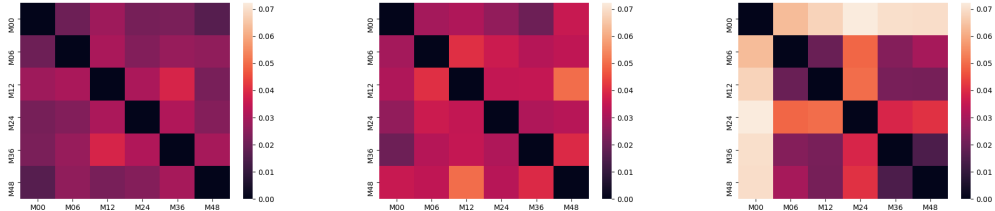


Figure 12: Topological evolution of a patient who transitions from MCI to AD in the course of the observation. For this particular case, the change in diagnosis occurred at $t = 24$, i.e. 24 months after the earliest available diagnosis, which also incidentally corresponds with the highest distance from that baseline.

4.1 Local persistence images are salient features for the characterization of atrophy due to AD

We obtain competitive performance results when classifying AD and CN subjects using persistence images obtained from patches, showing that the atrophy observed in AD can be characterized reasonably reliably from local persistence images (shown in Table 1). While the classification performance is lower than the state of the art reported in [Liu et al., 2018], which are about 85% to 90% and reported in Table 1, our results were obtained using a very simple neural architecture and only the local topological features of a single, small patch in the temporal lobe. Additionally, the standard deviation of our approach seems to be consistently lower than other approaches presented so far for which standard deviations of performance measures were available. This stability is likely because persistence homology itself is a stable method, robust to noise present in data [Cohen-Steiner et al., 2007], but this stability is also compounded by the fact that that persistence images have also been proven to be stable when introducing noise to the underlying persistence diagram Adams et al. [2017]. We note that one of the inherent impediments to our classifiers is that it does not have access to all the available clinical data contributing to the establishment of a formal diagnosis of Alzheimer’s disease. As per the revised guidelines for the diagnosis of AD, other factors such as blood and cerebrospinal fluid biomarkers and positron emission tomography (PET) scans also greatly influence the establishment of an AD diagnosis [McKhann et al., 2011].

Signs showing that our accuracy might be improved is that there is no increased ratio of topological outliers among the misclassified samples (Figure 14), nor is the proportion of patients showing a change in diagnosis substantially higher among misclassified samples, showing that patients who are oscillating between two diagnostic categories do not account for a high uncertainty. One way to increase the performance of our models would be a multi-patch setup, where the persistent image of other relevant patches could be considered. This stems from the fact that there is increasing evidence for the existence of biological subtypes of AD, which translate in differentially affected brain regions [Poulakis et al., 2018, Tijms et al., 2020]. In this context, computing the PI of other local areas of the brain which are affected by other subtypes of AD, like the precuneus, the medial and lateral temporal cortex, some of which incidentally also show increased accuracy in patch-based classification as seen in Figure 3. Another research avenue to be explored is the determination of possible weight functions applied to obtain persistence images to emphasize particularly important landmarks of Alzheimer’s disease. One might consider combining the results of a gradient-weighted class activation mapping (Grad-CAM) on a raw CNN trained on the patch with the persistence surface to increase the weight of particular topological features, should they stand out in the persistence image and yields better classification results.

4.2 Distances

As shown in Figure 9, the distribution of the distances of the persistent landscapes of each patch PL to the median PL for each of these diagnostic categories (shown in Figure 7) is very skewed, with some patients’ PL having a much higher distance values compared to the rest of the patients (see Table 2 and Figure 2). While the overall skew is most pronounced among MCI patients, pointing to a genuinely increased topological heterogeneity within this particular diagnostic category, some

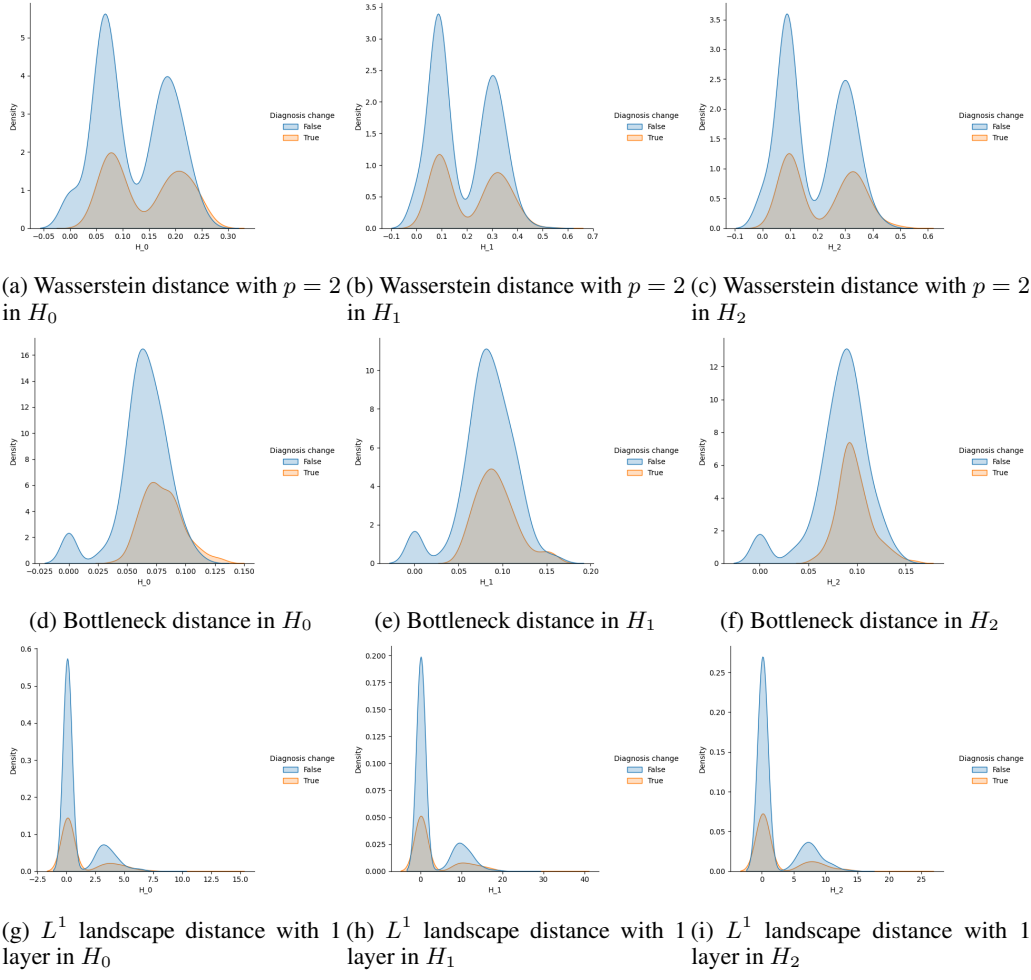


Figure 13: Kernel density estimation of the average average distance between each image timepoint for each patient. The orange curve represents all those patients who have had at least one change in diagnosis over the course of the disease, whereas patients who have not are within the blue curve.

of the more extreme values can be attributed to noise introduced at any step of the data acquisition and preprocessing steps described in section 2. Note that this phenomenon could also underlie the heterogeneity of the results we see in the comparisons made within a single patient (discussed below), indicating that noise probably plays a significant role in defining the distance among high persistence features obtained from one-layered persistence landscapes.

The aforementioned skewness and heterogeneity are most likely due to the high diversity of persistent topological features. As highlighted in section 1.2.2, the persistence landscape of a persistence diagrams provides a way to select the most persistent features for a given range of filtration values and given we have taken the first layer of a persistence landscape in our analyses, the topological heterogeneity mostly concerns the most persistent features. As noted in section 3.2.1, this heterogeneity disappears when performing the same type of analysis using persistence images as vectorized representations for the analysis. We hypothesize that this change is because persistence images consider all topological features, regardless of whether or not they are persistent. Hence, when considering all features, the distribution is mostly even, and topological outliers cannot be identified, save a few exceptions, namely AD patients in H_1 and H_2 .

Contrary to expectation, little appreciable difference was seen in intra-patient samples across distance functions. The reason for this lack of signal is likely because the level of noise introduced by averaging for each patient likely drown any intra-patient evolution. More sensitive clustering techniques using PDs could be more useful to determine the temporal trajectory of each patient. Additionally, the

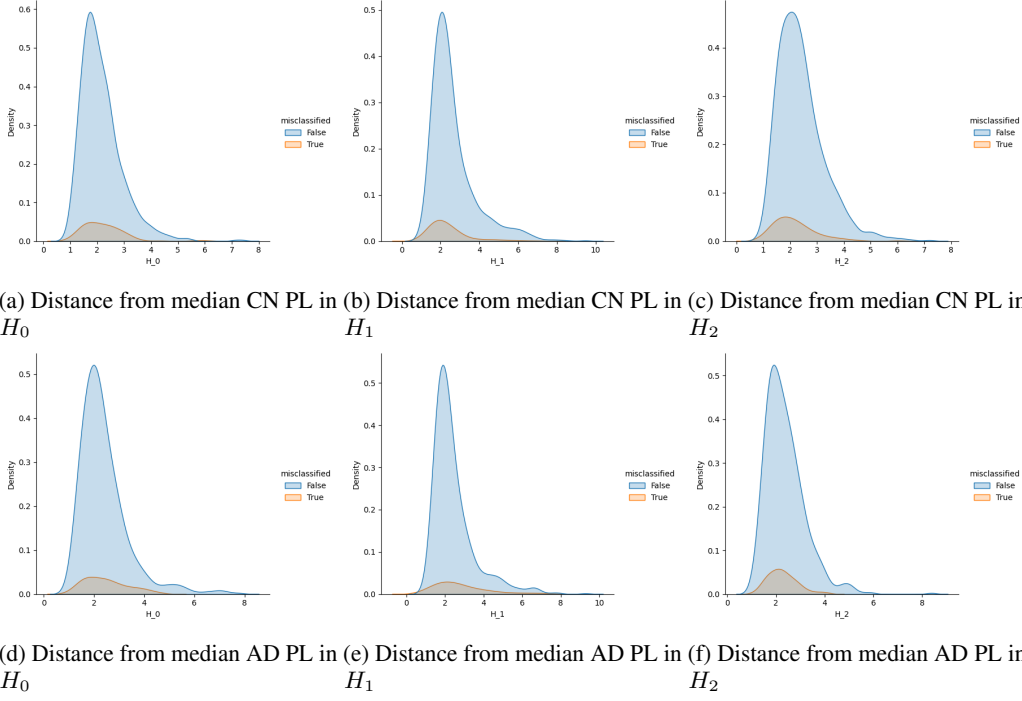


Figure 14: Kernel density estimation of distribution of the distance between the AD and CN median persistence image for images which have not and have been misclassified.

features extracted from a local patch are most likely not enough to characterize global atrophy progression patterns seen in the cortex of Alzheimer’s patients over time, as noted by [Toniolo et al., 2018].

4.3 Visualizing PIs using distances to the median PI of AD patients and CN subjects

We now examine Figure 15, which plots the principal components obtained from computing the L^1 norm of each image with respect to the median image in H_2 . We see some trends emerging: for instance, we tend to see CN PIs cluster in the upper part of the plot while AD PIs tend to cluster in the bottom, with MCI patients mostly blended in between. Yet, these trends are not clear enough to obtain clear clusters of disease phenotypes (i.e. one associated with each condition), let alone disease subtypes. Obtaining features more salient for clustering various subtypes would probably require more complex features, extracted for instance using a dynamic autoencoder on the persistence images [Mrabah et al., 2019]. Additionally, other methods tailored for topological features might also be developed and applied to this analysis pipeline.

4.4 Limitations and outlook

The first drawback of our analysis is the difficulty to highlight sources of noise in high persistence features. For instance, we mention in section 4.2 that some of the topological outliers that were highlighted in Figure 9 (but also observed among AD patients in Figure 15) could be due to noise, but the source of that noise is unknown. Specifically, it is not possible to investigate whether this noise comes from the preprocessing pipeline applied to it, or from the latent data distribution. We hypothesize that part of the noise could be introduced during the mapping of the original T1-weighted image to the reference normalized MNI space since it is the step that is most likely to introduce artificial noise in our data except the data itself [Collins, 1994], but it is impossible in the current setup to show evidence that this step in the preprocessing process is the root of the skewed distribution, or whether these changes can be attributed to intra-individual anatomical variance.

Another general limitation of the findings presented here is the coarseness of the analyses related to distances. While we wanted to get an insight into the rawest form of the data possible, taking

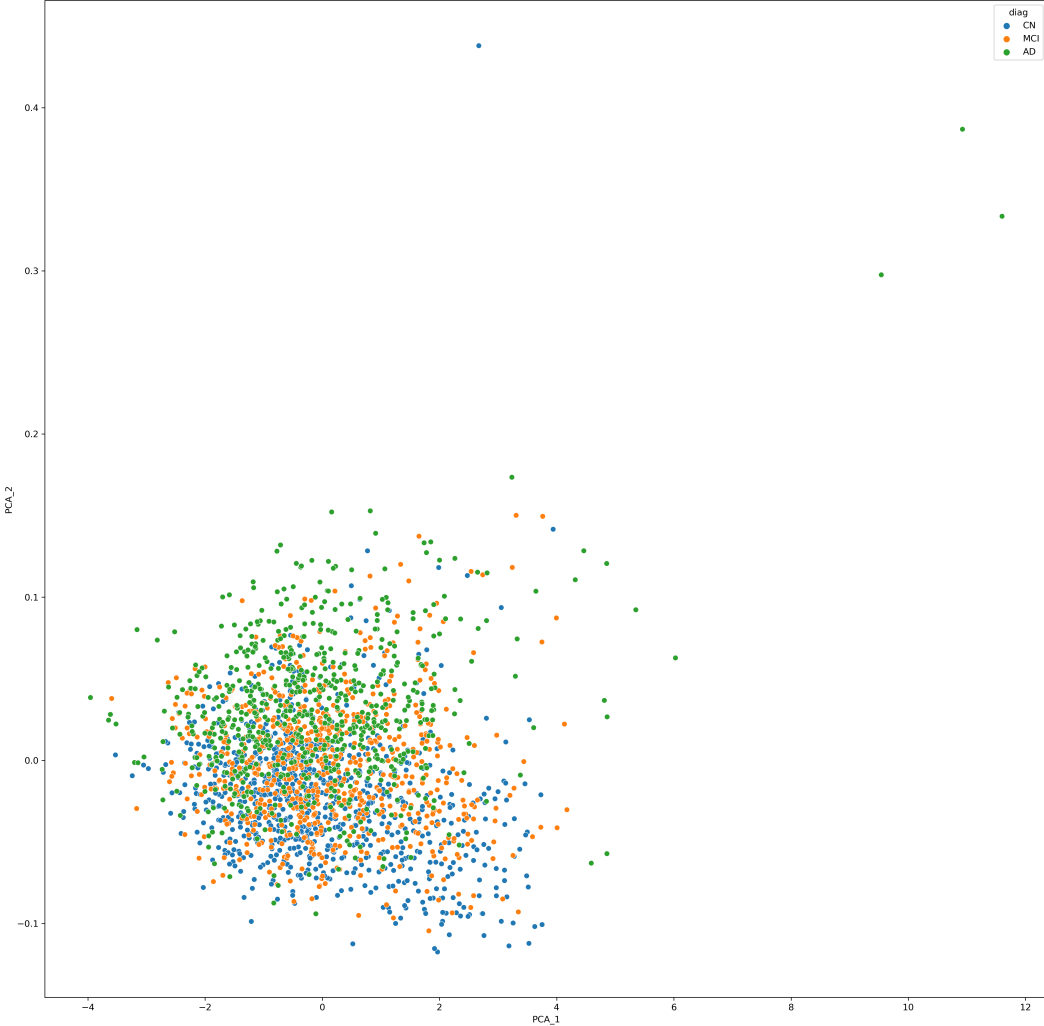


Figure 15: Visualisation of the two PCA components obtained from looking at the distance between the L^1 distance of each image to the median PI of AD and CN in H_2 .

the L^1 norm between some vector representations of the persistence diagram for instance can artificially drown highly discriminatory features. Therefore, the potential of the topological features to discriminate between patients who progress from a baseline diagnosis or not can be further investigated using more optimized clustering techniques making use of the topological features extracted using persistent homology.

More specifically, some coarseness was deliberately introduced by extracting only one layer when analyzing persistence landscapes. This value was chosen because we are interested in changes in the highly persistent features of the data, hence eliminating the noise arising from the persistent homology computation. On a similar note, the performance of our classifier could have further be optimized using a deeper and more optimized architecture, but the choice of a simple architecture was made to assess the saliency of the data rather than the potential of the classifier itself to yield good results with little computation.

Our classification task does not cover the full spectrum of all of the possible diagnoses a patient coming to a memory clinic might present. Importantly, our model was not trained to classify patients who have a case of MCI, which is neither AD nor CN, but in between. The discriminatory power of the features used in this report do not enable the full-fledged diagnostic classification task required in the clinic. Further studies need to also assess the saliency of the PI obtained from the temporal patch

in question for a better assessment of the clinical usefulness of persistent homology in classifying the various categories of patients.

Despite these limitations, it is important to point out that the approach outlined here was specifically aimed at analyzing MRI images obtained from patients with Alzheimer’s disease, it could also be applied to any other neurodegenerative disorder. Other prevalent neurodegenerative disorders include Parkinson’s disease, dementia with Lewy bodies, and genetically inherited diseases like Huntington’s disease, which all have distinct atrophy patterns and therefore distinct topological signatures. Adaptations would be required, such as adapting the choice of a patch of interest – as an example, it might be more relevant to look at the basal ganglia for Huntington’s disease, since the medial temporal lobe is observed to be mostly spared in Huntington’s [Kuhl et al., 1982, Halliday et al., 1998, Kassubek et al., 2004].

Additionally, we note that a clustering using topological descriptors could be used to more finely delineate subtypes of AD and various stages of progression. For instance, using deep clustering techniques and embeddings using persistence images as inputs could yield useful insights into the various stages of progression and subtypes of dementia. These more sensitive methods could then, once fine-tuned, hopefully also track preclinical stages of AD, when atrophy is present but does not result in cognitive decline due to the presence of a cognitive reserve [Scarmeas and Stern, 2004, van Loenhoud et al., 2017]. The identification of patient populations at risk of developing the disease could then form the target of any potential preventive treatment.

5 Conclusions

In this report we have shown that PIs computed from a patch in the temporal lobe are salient for classifying CN and AD subjects. Additionally, we show that the distribution of distances among the patients in each of the diagnostic category is skewed, indicating the presence of topological outliers, but, overall, does not affect the classification performance. Then, we show a significant, but not substantial, increase in distance among images belonging to a given patient who deteriorates towards Alzheimer’s disease versus patients who do not. Our last finding is that clustering patients solely according to their distance with respect to multiple median PI does not allow proper AD subtype identification. Although promising, all of these topology-driven approaches need further development to maximize the information that can be extracted from MRI images.

References

- WHO. Global action plan on the public health response to dementia 2017–2025. 2017.
- Katherine E Sleeman, Maja de Brito, Simon Etkind, Kennedy Nkhoma, Ping Guo, Irene J Higginson, Barbara Gomes, and Richard Harding. The escalating global burden of serious health-related suffering: projections to 2060 by world regions, age groups, and health conditions. *The Lancet Global Health*, 7(7):e883–e892, 2019.
- Guy M McKhann, David S Knopman, Howard Chertkow, Bradley T Hyman, Clifford R Jack Jr, Claudia H Kawas, William E Klunk, Walter J Koroshetz, Jennifer J Manly, Richard Mayeux, et al. The diagnosis of dementia due to alzheimer's disease: recommendations from the national institute on aging-alzheimer's association workgroups on diagnostic guidelines for alzheimer's disease. *Alzheimer's & dementia*, 7(3):263–269, 2011.
- Lieke L Smits, Yolande AL Pijnenburg, Esther LGE Koedam, Annelies E van der Vlies, Ilona EW Reuling, Teddy Koene, Charlotte E Teunissen, Philip Scheltens, and Wiesje M van der Flier. Early onset alzheimer's disease is associated with a distinct neuropsychological profile. *Journal of Alzheimer's Disease*, 30(1):101–108, 2012.
- Sylvain Lehmann and Charlotte Elisabeth Teunissen. Biomarkers of alzheimer's disease: The present and the future. *Frontiers in Neurology*, 7:158, 2016.
- William G Tharp and Indra Neil Sarkar. Origins of amyloid- β . *BMC genomics*, 14(1):1–15, 2013.
- Tamas Fulop, Jacek M Witkowski, Karine Bourgade, Abdelouahed Khalil, Echarki Zerif, Anis Larbi, Katsuiku Hirokawa, Graham Pawelec, Christian Bocti, Guy Lacombe, et al. Can an infection hypothesis explain the beta amyloid hypothesis of alzheimer's disease? *Frontiers in aging neuroscience*, 10:224, 2018.
- Ji-Yeon Hur, Georgia R Frost, Xianzhong Wu, Christina Crump, Si Jia Pan, Eitan Wong, Marilia Barros, Thomas Li, Pengju Nie, Yujia Zhai, et al. The innate immunity protein ifitm3 modulates γ -secretase in alzheimer's disease. *Nature*, pages 1–6, 2020.
- Sandro Dá Mesquita, Ana Catarina Ferreira, João Carlos Sousa, Margarida Correia-Neves, Nuno Sousa, and Fernanda Marques. Insights on the pathophysiology of alzheimer's disease: The crosstalk between amyloid pathology, neuroinflammation and the peripheral immune system. *Neuroscience & Biobehavioral Reviews*, 68:547–562, 2016.
- Michel Goedert and Maria Grazia Spillantini. A century of alzheimer's disease. *science*, 314(5800): 777–781, 2006.
- Giovanni B Frisoni, Nick C Fox, Clifford R Jack, Philip Scheltens, and Paul M Thompson. The clinical use of structural mri in alzheimer disease. *Nature Reviews Neurology*, 6(2):67–77, 2010.
- Lorenzo Pini, Michela Pievani, Martina Bocchetta, Daniele Altomare, Paolo Bosco, Enrica Cavedo, Samantha Galluzzi, Moira Marizzoni, and Giovanni B Frisoni. Brain atrophy in alzheimer's disease and aging. *Ageing research reviews*, 30:25–48, 2016.
- Junhao Wen, Elina Thibeau-Sutre, Mauricio Diaz-Melo, Jorge Samper-González, Alexandre Routier, Simona Bottani, Didier Dormont, Stanley Durrleman, Ninon Burgos, Olivier Colliot, et al. Convolutional neural networks for classification of alzheimer's disease: Overview and reproducible evaluation. *Medical Image Analysis*, page 101694, 2020.
- Konstantinos Poulakis, Joana B Pereira, Patrizia Mecocci, Bruno Vellas, Magda Tsolaki, Iwona Kłoszewska, Hilkka Soininen, Simon Lovestone, Andrew Simmons, Lars-Olof Wahlund, et al. Heterogeneous patterns of brain atrophy in alzheimer's disease. *Neurobiology of aging*, 65:98–108, 2018.
- Betty M Tijms, Johan Gobom, Lianne Reus, Iris Jansen, Shengjun Hong, Valerija Dobricic, Fabian Kilpert, Mara ten Kate, Frederik Barkhof, Magda Tsolaki, et al. Pathophysiological subtypes of alzheimer's disease based on cerebrospinal fluid proteomics. *medRxiv*, 2020.
- Henri Poincaré. *Analysis situs*. Gauthier-Villars, 1895.

- Ioan Mackenzie James. *History of topology*. Elsevier, 1999.
- Tamal K Dey, Herbert Edelsbrunner, and Sumanta Guha. Computational topology. *Contemporary mathematics*, 223:109–144, 1999.
- Robert Ghrist. Barcodes: the persistent topology of data. *Bulletin of the American Mathematical Society*, 45(1):61–75, 2008.
- Erik J Amézquita, Michelle Y Quigley, Tim Ophelders, Elizabeth Munch, and Daniel H Chitwood. The shape of things to come: Topological data analysis and biology, from molecules to organisms. *Developmental Dynamics*, 2020.
- Daniel Freedman and Chao Chen. Algebraic topology for computer vision. *Computer Vision*, pages 239–268, 2009.
- Herbert Edelsbrunner and John Harer. *Computational topology: an introduction*. American Mathematical Soc., 2010.
- Henry Adams, Tegan Emerson, Michael Kirby, Rachel Neville, Chris Peterson, Patrick Shipman, Sofya Chepushtanova, Eric Hanson, Francis Motta, and Lori Ziegelmeier. Persistence images: A stable vector representation of persistent homology. *The Journal of Machine Learning Research*, 18(1):218–252, 2017.
- Peter Bubenik. Statistical topological data analysis using persistence landscapes. *The Journal of Machine Learning Research*, 16(1):77–102, 2015.
- Peter Bubenik. The persistence landscape and some of its properties. In *Topological Data Analysis*, pages 97–117. Springer, 2020.
- Jesse J Berwald, Joel M Gottlieb, and Elizabeth Munch. Computing wasserstein distance for persistence diagrams on a quantum computer. *arXiv preprint arXiv:1809.06433*, 2018.
- Serge Gauthier, Barry Reisberg, Michael Zaudig, Ronald C Petersen, Karen Ritchie, Karl Broich, Sylvie Belleville, Henry Brodaty, David Bennett, Howard Chertkow, et al. Mild cognitive impairment. *The lancet*, 367(9518):1262–1270, 2006.
- Clifford R Jack Jr, Matt A Bernstein, Nick C Fox, Paul Thompson, Gene Alexander, Danielle Harvey, Bret Borowski, Paula J Britson, Jennifer L. Whitwell, Chadwick Ward, et al. The alzheimer’s disease neuroimaging initiative (adni): Mri methods. *Journal of Magnetic Resonance Imaging: An Official Journal of the International Society for Magnetic Resonance in Medicine*, 27(4):685–691, 2008.
- Sarah C Brüningk, Felix Hensel, Catherine R Jutzeler, and Bastian Rieck. Image analysis for alzheimer’s disease prediction: Embracing pathological hallmarks for model architecture design. *arXiv preprint arXiv:2011.06531*, 2020.
- Guillaume Tauzin, Umberto Lupo, Lewis Tunstall, Julian Burella Pérez, Matteo Caorsi, Anibal Medina-Mardones, Alberto Dassatti, and Kathryn Hess. giotto-tda: A topological data analysis toolkit for machine learning and data exploration, 2020.
- François Fleuret et al. Keras. <https://keras.io>, 2015.
- Henry B Mann and Donald R Whitney. On a test of whether one of two random variables is stochastically larger than the other. *The annals of mathematical statistics*, pages 50–60, 1947.
- Mingxia Liu, Jun Zhang, Dong Nie, Pew-Thian Yap, and Dinggang Shen. Anatomical landmark based deep feature representation for mr images in brain disease diagnosis. *IEEE journal of biomedical and health informatics*, 22(5):1476–1485, 2018.
- David Cohen-Steiner, Herbert Edelsbrunner, and John Harer. Stability of persistence diagrams. *Discrete & computational geometry*, 37(1):103–120, 2007.
- Sofia Toniolo, Laura Serra, Giusy Olivito, Camillo Marra, Marco Bozzali, and Mara Cercignani. Patterns of cerebellar gray matter atrophy across alzheimer’s disease progression. *Frontiers in Cellular Neuroscience*, 12:430, 2018.

Nairouz Mrabah, Naimul Mefraz Khan, Riadh Ksantini, and Z Lachiri. Deep clustering with a dynamic autoencoder. *CoRR*, 2019.

D Louis Collins. 3d model-based segmentation of individual brain structures from magnetic resonance imaging data. 1994.

David E Kuhl, Michael E Phelps, Charles H Markham, E Jeffrey Metter, Walter H Riege, and James Winter. Cerebral metabolism and atrophy in huntington's disease determined by 18fdg and computed tomographic scan. *Annals of Neurology: Official Journal of the American Neurological Association and the Child Neurology Society*, 12(5):425–434, 1982.

GM Halliday, DA McRitchie, V Macdonald, KL Double, RJ Trent, and E McCusker. Regional specificity of brain atrophy in huntington's disease. *Experimental neurology*, 154(2):663–672, 1998.

J Kassubek, FD Juengling, T Kioschies, K Henkel, J Karitzky, B Kramer, D Ecker, J Andrich, C Saft, P Kraus, et al. Topography of cerebral atrophy in early huntington's disease: a voxel based morphometric mri study. *Journal of Neurology, Neurosurgery & Psychiatry*, 75(2):213–220, 2004.

Nikolaos Scarmeas and Yaakov Stern. Cognitive reserve: implications for diagnosis and prevention of alzheimer's disease. *Current neurology and neuroscience reports*, 4(5):374–380, 2004.

Anna C van Loenhoud, Alle Meije Wink, Colin Groot, Sander CJ Verfaillie, Jos Twisk, Frederik Barkhof, Bart van Berckel, Philip Scheltens, Wiesje M van der Flier, and Rik Ossenkoppele. A neuroimaging approach to capture cognitive reserve: application to alzheimer's disease. *Human brain mapping*, 38(9):4703–4715, 2017.

A Supplements

A.1 Preprocessing of MRI data

We included all T1-weighted MRI images from ADNI 1, 2, 3, and GO, which were captured and preprocessed by ADNI. Results included in our work come from preprocessing performed using fMRIprep 20.1.1, a Nipype 1.5.0 based tool. All MRIs were corrected for intensity non-uniformity (INU) with N4BiasFieldCorrection, distributed with ANTs 2.2.0, and used as T1w-reference throughout the workflow. The T1w-reference was then skull-stripped with a Nipype implementation of the antsBrainExtraction.sh workflow (from ANTs), using OASIS30ANTS as a target template. Volume-based spatial normalisation to a standard coordinate space (MNI152NLin2009cAsym) was performed through nonlinear registration with antsRegistration, using brain-extracted versions of both T1w reference and the T1w template. We selected the template ‘ICMB 152 Nonlinear Asymmetrical Template Version 2009c’ for spatial normalisation. Many internal operations of fMRIprep use the NiLearn library, version 0.6.2, , mostly within the functional processing workflow. For more details of the pipeline, please refer to [the official documentation of fMRIprep](#). Preprocessing was finalized by intensity normalization of the extracted and MNI space registered brain images.